J. Fluid Mech. (1994), vol. 273, pp. 141–168

The spatial structure of neutral atmospheric surface-layer turbulence

By JAKOB MANN

Risø National Laboratory, 4000 Roskilde, Denmark

(Received 7 July 1992 and in revised form 21 February 1994)

Modelling of the complete second-order structure of homogeneous, neutrally stratified atmospheric boundary-layer turbulence, including spectra of all velocity components and cross-spectra of any combination of velocity components at two arbitrarily chosen points, is attempted. Two models based on Rapid Distortion Theory (RDT) are investigated. Both models assume the velocity profile in the height interval of interest to be approximately linear. The linearized Navier–Stokes equation together with considerations of 'eddy' lifetimes are then used to modify the spatial second-order structure of the turbulence. The second model differs from the first by modelling the blocking by the surface in addition to the shear. The resulting models of the spectral velocity tensor contain only three adjustable parameters: a lengthscale describing the size of the largest energy-containing eddies, a non-dimensional number used in the parametrization of 'eddy' lifetime, and the third parameter is a measure of the energy dissipation.

Two atmospheric experiments, both designed to investigate the spatial structure of turbulence and both running for approximately one year, are used to test and calibrate the models. Even though the approximations leading to the models are very crude they are capable of predicting well the two-point second-order statistics such as cross-spectra, coherences and phases, on the basis of measurements carried out at one point. The two models give very similar predictions, the largest difference being in the coherences involving vertical velocity fluctuations, where the blocking by the surface seems to have a significant effect.

1. Introduction

Knowledge of the turbulent atmospheric wind field has become important in the calculation of dynamic loads on some spatially extended structures, such as large bridges, towers and wind turbines. For many of these structures the cross-spectra of wind fluctuations at different points on the structure are paramount in the estimation of dynamic wind loads. Under some simplifying circumstances the spectrum of the modal forces on the structure can be written as weighted integrals of the cross-spectra. According to Davenport (1977) the weights include modal amplitude and drag or lift coefficients at different points of the structure. For more complicated structures with moving parts or in the case of nonlinear structural responses there is not a similarly simple relation between spectral characteristics of the flow and the forces. However, in these cases also the cross-spectra are important for the description of dynamic loads.

For some structures the streamwise wind component of the turbulent flow is

important while for others the vertical velocity fluctuations give rise to loads. There may even be structures where combinations of velocity fluctuations in different directions at different points are of importance. It is therefore desirable to have a unified description of the complete two-point second-order structure of the turbulence, i.e. cross-spectra of arbitrary wind components at two arbitrarily chosen points.

Many experiments have been carried out in order to measure the spectral characteristics of the turbulence at the lowest ≈ 100 m of the atmosphere (Panofsky & Dutton 1984). Most reported observations concern one-point spectra and there is a general agreement on the shapes of these, except at the lowest frequencies. In this paper we shall investigate two models of the spectral velocity tensor, $\Phi_{ij}(\boldsymbol{k})$, for horizontally homogeneous, atmospheric surface-layer turbulence for neutral stratification, which prevails at high wind speeds.

The basis of the models is *rapid distortion theory* (RDT), which implies a linearization of the Navier–Stokes equation. The models combine RDT with considerations about eddy lifetimes. The difference between the two models is that the first assumes a uniform shear, while the second in addition to the effects of shear also tries to take into account the blocking by the surface by inhomogeneous RDT (Hunt & Graham 1978; Gartshore, Durbin & Hunt 1983; Lee & Hunt 1989, see figure 2). The first model is abbreviated US, the second US+B.

Owing to the difficulties in solving the Navier–Stokes equation the physical and mathematical approximations are quite crude. Therefore, the models have been calibrated and checked with data from two large experiments. In the first, turbulence was measured over water in connection with estimation of wind loads on what is going to be the world's largest suspension bridge (Mann, Kristensen & Courtney 1991; Larsen 1992). The second experiment investigated turbulence structure over a rural area in Denmark in connection with wind loads on horizontal-axis wind turbines (Courtney 1988).

In § 2 we define the notation, discuss symmetries of different tensor models and briefly describe the isotropic tensor with the von Kármán energy spectrum on which the models in § 3 are based. Then in § 3 we present the tensor models, which have only three parameters: a lengthscale, a constant connected to the 'lifetime' of the eddies, and a measure of the energy dissipation. Finally, in § 4, we compare the two models with data by adjusting the three parameters to fit the one-point spectra and predicting the measured two-point cross-spectra.

2. Preliminaries

We present the basic definitions and notation together with some properties of the isotropic tensor which are needed.

2.1. *Definitions*

The turbulent velocity field $\tilde{\boldsymbol{u}}(\boldsymbol{x})$ is assumed to be incompressible, and the fluctuations, $\boldsymbol{u}(\boldsymbol{x}) = \tilde{\boldsymbol{u}}(\boldsymbol{x}) - \boldsymbol{U}(\boldsymbol{x})$, about the mean wind field, $\boldsymbol{U}(\boldsymbol{x})$, are, except for the model in § 3.3, homogeneous in space. Therefore the covariance tensor

$$R_{ij}(\boldsymbol{r}) = \langle u_i(\boldsymbol{x}) u_j(\boldsymbol{x}+\boldsymbol{r}) \rangle , \tag{2.1}$$

where $\langle\ \rangle$ denotes ensemble averaging, is only a function of the separation vector $\boldsymbol{r}$. From (2.1) it follows that

$$R_{ij}(\boldsymbol{r}) = R_{ji}(-\boldsymbol{r}). \tag{2.2}$$

For the components of the position vector in space, $\boldsymbol{x} = (x_1, x_2, x_3)$, we shall often use (x, y, z) or $(\Delta x, \Delta y, \Delta z)$ to denote position differences and for the components of the velocity fluctuations, $\boldsymbol{u} = (u_1, u_2, u_3)$, we sometimes use (u, v, w). Some assumption of homogeneity is unavoidable if we want the mathematics to be relatively simple. In this paper we model the Fourier transform of (2.1), *the spectral velocity tensor*:

$$\Phi_{ij}(\boldsymbol{k}) = \frac{1}{(2\pi)^3} \int R_{ij}(\boldsymbol{r}) \exp(-\mathrm{i}\boldsymbol{k} \cdot \boldsymbol{r}) \mathrm{d}\boldsymbol{r}, \tag{2.3}$$

where $\int \mathrm{d}\boldsymbol{r} \equiv \int_{-\infty}^{\infty} \int_{-\infty}^{\infty} \int_{-\infty}^{\infty} \mathrm{d}r_1 \mathrm{d}r_2 \mathrm{d}r_3$. Denoting complex conjugation by *, we see that (2.2) implies that $\Phi_{ij} = \Phi_{ji}^*$, i.e. the tensor is Hermitian.

Not only the Fourier transform of the covariance tensor is of interest but also the Fourier transform of the velocity field itself. Since the stochastic velocity field is not square integrable over all physical space we can represent the field in terms of a generalized stochastic Fourier–Stieltjes integral:

$$\boldsymbol{u}(\boldsymbol{x}) = \int \mathrm{e}^{\mathrm{i}\boldsymbol{k}\cdot\boldsymbol{x}} \mathrm{d}\boldsymbol{Z}(\boldsymbol{k}), \tag{2.4}$$

where the integration is over all wavenumber space (Batchelor 1953). From homogeneity of the velocity fluctuations it follows that the stochastic vector field $\boldsymbol{Z}(\boldsymbol{k})$ has uncorrelated increments, i.e. $\langle \mathrm{d}Z_i(\boldsymbol{k}') \mathrm{d}Z_j^*(\boldsymbol{k}'') \rangle = 0$ for $\boldsymbol{k}' \neq \boldsymbol{k}''$. The process $\boldsymbol{Z}$ is connected to the spectral tensor by

$$\frac{\langle \mathrm{d}Z_i^*(\boldsymbol{k}) \mathrm{d}Z_j(\boldsymbol{k}) \rangle}{\mathrm{d}k_1 \mathrm{d}k_2 \mathrm{d}k_3} = \Phi_{ij}(\boldsymbol{k}), \tag{2.5}$$

which is valid for infinitely small $\mathrm{d}k_i$†. The representation (2.4) may also form the basis for a numerical simulation of a turbulent wind field assuming the stochastic vector field $\boldsymbol{Z}(\boldsymbol{k})$ to be Gaussian and to have independent increments. A good introduction to the spectral tensor and its physical significance may be found in Tennekes & Lumley (1972).

An alternative to the spectral tensor is the set of all cross-spectra

$$\chi_{ij}(k_1, \Delta y, \Delta z) = \frac{1}{2\pi} \int_{-\infty}^{\infty} R_{ij}(x, \Delta y, \Delta z) \exp(-\mathrm{i}k_1 x) \mathrm{d}x \tag{2.6}$$

which contains the same information and which is most often used in practical applications, such as estimation of loads on structures. The connection between the components of the spectral tensor and the cross-spectra is

$$\chi_{ij}(k_1, \Delta y, \Delta z) = \int \Phi_{ij}(\boldsymbol{k}) \exp(\mathrm{i}(k_2 \Delta y + k_3 \Delta z)) \mathrm{d}\boldsymbol{k}_\perp, \tag{2.7}$$

where $\int \mathrm{d}\boldsymbol{k}_\perp \equiv \int_{-\infty}^{\infty} \int_{-\infty}^{\infty} \mathrm{d}k_2 \mathrm{d}k_3$ (Lumley 1970, chapter 4).

Besides the cross-spectrum the *coherence* or *spectral coherence*

$$\mathrm{coh}_{ij}(k_1, \Delta y, \Delta z) = \frac{|\chi_{ij}(k_1, \Delta y, \Delta z)|^2}{F_i(k_1) F_j(k_1)} \qquad \text{(no summation)}, \tag{2.8}$$

where $F_i(k_1) = \chi_{ii}(k_1, 0, 0)$ (no summation) is the one-point spectrum, is often reported

† Other widely used ways to represent the velocity field are either as a Fourier series assuming the field to obey cyclic boundary conditions on a box in space much larger than the scales of interest (Townsend 1976), or assuming the velocity field to vanish outside a large box. The mathematical differences of these approaches are not of interest here.

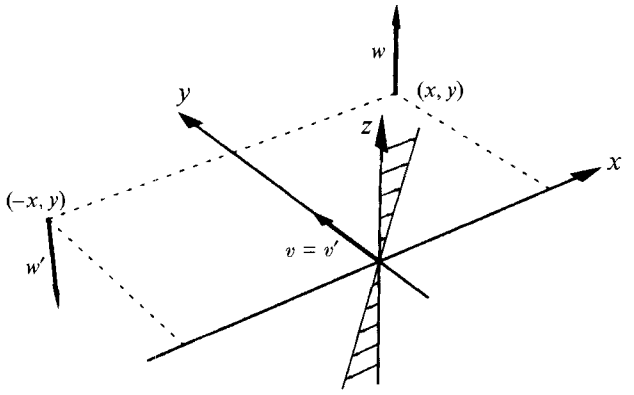

FIGURE 1. Coordinate system with the linear shear profile (2.13) shown along the z-axis. The vector v is the transversal component at the point $(0,0)$ and w is the vertical component at (x,y) of a turbulent velocity field. The vectors v' and w' are the same components after a rotation of 180° about the y-axis of the field.

in the literature. Sometimes the coherence is defined as the square root of the expression above. The phase, φ_{ij}, is defined as

$$\chi_{ij}(k_1, \Delta y, \Delta z) = |\chi_{ij}(k_1, \Delta y, \Delta z)| \exp\left(\mathrm{i}\varphi_{ij}(k_1, \Delta y, \Delta z)\right) \qquad \text{(no summation)} \qquad (2.9)$$

and we note that from (2.7) and $\Phi_{ij} = \Phi^*_{ji}$ we get $\varphi_{ij}(k_1, \Delta y, \Delta z) = -\varphi_{ji}(k_1, -\Delta y, -\Delta z)$.

According to the definitions used here the (co-)variances can be expressed as

$$\langle u_i u_j \rangle = \langle u_i(\boldsymbol{x}) u_j(\boldsymbol{x}) \rangle = \int_{-\infty}^{\infty} \chi_{ij}(k_1) \mathrm{d}k_1 = \int \Phi_{ij}(\boldsymbol{k}) \mathrm{d}\boldsymbol{k}. \qquad (2.10)$$

With these conventions the (cross-)spectra $\chi_{ij}(k_1) = \chi_{ij}(k_1, 0, 0)$ are often called two-sided.

2.2. *Symmetries*

From symmetries of the spectral tensor it is possible to determine if some cross-spectra are real, purely imaginary or zero. Furthermore, they can be exploited in the numerical calculation of $\chi_{ij}(k_1)$ from $\Phi_{ij}(\boldsymbol{k})$.

We define the (second-order) symmetry group of a turbulent field as the group of reflections and rotations of the space which leaves the statistics of the turbulent field unchanged. More precisely the symmetry group of a (stochastic) turbulent field is the subgroup of transformations $\boldsymbol{T}$ in the group of all orthonormal transformations in $\mathbf{R}^3$ for which the second-order statistics of $u_i(\boldsymbol{x})$ are the same as $T_{ij}u_j(\boldsymbol{Tx})$ (summation over repeated indices is understood). For the covariance tensor this means that

$$\begin{aligned} R_{ij}(\boldsymbol{r}) &= \langle u_i(\boldsymbol{x}) u_j(\boldsymbol{x} + \boldsymbol{r}) \rangle \\ &= \langle T_{il} u_l(\boldsymbol{Tx}) T_{jk} u_k(\boldsymbol{Tx} + \boldsymbol{Tr}) \rangle = T_{il} R_{lk}(\boldsymbol{Tr}) T_{jk} \end{aligned} \qquad (2.11)$$

for transformations in the symmetry group. Since the absolute value of the determinant of $\boldsymbol{T}$ is one we get, using the definition (2.3), for the spectral tensor

$$\Phi_{ij}(\boldsymbol{k}) = T_{il} \Phi_{lk}(\boldsymbol{T}^* \boldsymbol{k}) T_{jk}, \qquad (2.12)$$

where $\boldsymbol{T}^*$ is the adjoint of $\boldsymbol{T}$ (i.e. the transposed matrix).

For the models developed in § 3 the mean wind field is assumed to be well

represented by a uniform shear with the flow in the x_1-direction:

$$\boldsymbol{U}(\boldsymbol{x}) = \langle \tilde{\boldsymbol{u}}(\boldsymbol{x}) \rangle = z \frac{\mathrm{d}U}{\mathrm{d}z} \boldsymbol{e}_1, \tag{2.13}$$

and the fluctuations are distorted by this shear†. The following symmetries apply to this situation. Firstly, for both the US and US+B models, there must be left-right symmetry (since we ignore the rotation of the of the Earth). Secondly, the US model is unaffected by a rotation of 180° about the x_2-axis and thus, ignoring the effect of gravity, the fluctuating field has this symmetry. Therefore, the symmetry group for the US model consists of four elements:

$$\left\{ \boldsymbol{I}, \begin{pmatrix} 1 & 0 & 0 \\ 0 & -1 & 0 \\ 0 & 0 & 1 \end{pmatrix}, \begin{pmatrix} -1 & 0 & 0 \\ 0 & 1 & 0 \\ 0 & 0 & -1 \end{pmatrix}, -\boldsymbol{I} \right\} \tag{2.14}$$

where $\boldsymbol{I}$ is the identity matrix. From the last element, $-\boldsymbol{I}$, it follows from (2.12) and (2.3) that $\boldsymbol{\Phi}$ is real and since it is Hermitian it is also symmetric. From the definition (2.6) and (2.11) we get, using the third element of the symmetry group, that $\chi_{ij}(k_1, y, 0)$ is purely imaginary for $\{i,j\} = \{1,2\}$ or $\{2,3\}$ and real otherwise. The case $\{i,j\} = \{2,3\}$ is shown in figure 1. The statistics of the turbulent field must be unchanged after a rotation of 180° about the y-axis, i.e. $\langle vw \rangle = \langle v'w' \rangle$ or $R_{23}(x,y,0) = -R_{23}(-x,y,0)$. From this relation and (2.6) it follows that the cross-spectrum $\chi_{23}(k_1, \Delta y, 0)$ is purely imaginary or equivalently that $\varphi_{23}(k_1, \Delta y, 0) = \pm 90°$. An example of a measured phase is shown in figure 9. Similarly, using the second element of the symmetry group one can prove that $\chi_{ij}(k_1, 0, \Delta z)$ is zero for $\{i,j\} = \{1,2\}$ or $\{2,3\}$.

It should be noted that the third (and thereby also the last) element in the symmetry group is in fact only approximately valid in the neutral atmospheric boundary layer since the velocity profile is not linear but rather logarithmic because of the presence of the surface of the Earth. We therefore expect a model based on this symmetry group only to be valid for eddies of linear dimension smaller than the length over which the shear changes appreciably. A theory based on a logarithmic profile would be too complicated mathematically for us to deal with. (See Hunt *et al.* 1989 for an analysis of correlations and lengthscales in this case.) As a compromise we introduce the US+B model in § 3.3 which also has uniform shear but breaks the 180° symmetry about the y-axis by modelling the blocking by the surface.

Related to the nonlinear velocity profile a non-zero skewness of the w-component would also show that the 180° rotation about the y-axis is not a perfect symmetry. Measurements of $S_w \equiv \langle w^3 \rangle / \sigma_w^3$ in the neutral surface layer from the Kansas experiment gives values between 0.1 and 0.2 (Izumi 1971) with higher values to the unstable side and lower values around zero to the stable side. We measure the skewness, S_w, to be 0.27 and −0.12 for the Great Belt Coherence Experiment (§ 4.2) and LAMEX (§ 4.3), respectively. Large-eddy simulations (LES) of the neutral boundary layer give small negative skewnesses close to the surface (C.-H. Moeng, 1993, private communication); however, as pointed out by Moeng, in the surface layer LES may not resolve the motions sufficiently to predict the skewness. These limitations of LES have been discussed in Schmidt & Schumann (1989).

The group of symmetries of *axisymmetric turbulence* is all rotations about the axis of symmetry together with reflections in planes containing the axis and in the plane

† For neatness, we have here chosen $\boldsymbol{U}(\boldsymbol{0}) = \boldsymbol{0}$. We could have chosen, say, $\boldsymbol{U}(\boldsymbol{0}) = U_0 \boldsymbol{e}_1$; it is just a matter of defining of the origin of the z-axis. The theories presented in § 3 (US) only depend on the shear, not on the mean wind speed at the origin.

perpendicular to the axis. A model of axisymmetric turbulence has been developed by Chandrasekhar (1950) (also described in detail by Sreenivasan & Narasimha 1978) and if the axis is vertical it is thought to give a good representation of convective turbulence without shear. However, vertical axisymmetry implies $\sigma_u^2 = \sigma_v^2$ which is not observed for atmospheric surface-layer turbulence at high wind speeds.

Inspired by the axisymmetric tensor Kristensen *et al.* (1989) proposed a spectral tensor model with the following symmetry group:

$$\begin{pmatrix} \pm 1 & 0 & 0 \\ 0 & \pm 1 & 0 \\ 0 & 0 & \pm 1 \end{pmatrix}. \tag{2.15}$$

By introducing 7 independent parameters defining various functions in their model Kristensen *et al.* could fit $F_1(k_1)$, $F_2(k_1)$ and $F_3(k_1)$, the measured one-point spectra of along wind, transversal and vertical wind fluctuations, respectively, fairly well and thereby also giving the right proportions of the variances and the lengthscales of all three components. The calculated coherences, however, generally overestimated the measured coherences when the distance between the anemometers was not small compared to the height above the surface. Furthermore, reflection in the horizontal plane which is an element in (2.15) implies $\chi_{13}(k_1, 0, 0) = 0$ and $\varphi_{11}(k_1, 0, \Delta z) = 0$ which is not supported by data.

2.3. *Taylor's hypothesis*

Usually Taylor's hypothesis is used to convert measured time series into 'space series'. When the shear is zero the mean speed at all points in space is the same and the hypothesis can be straightforwardly applied to interpret two-point time spectra as space cross-spectra. When the shear is not zero, however, Taylor's hypothesis is not so easily applicable. Consequently it will be used heuristically as follows. Consider two points $\boldsymbol{x}_1$ and $\boldsymbol{x}_2$ with $\boldsymbol{x}_2 - \boldsymbol{x}_1$ perpendicular to $\boldsymbol{U}(\boldsymbol{x})$. Simultaneously measured time series $\tilde{\boldsymbol{u}}(\boldsymbol{x}_1, t)$ and $\tilde{\boldsymbol{u}}(\boldsymbol{x}_2, t)$ are interpreted as the wind field along two lines in space: $\tilde{\boldsymbol{u}}(\boldsymbol{x}_1 - \boldsymbol{U}_m t, 0)$ and $\tilde{\boldsymbol{u}}(\boldsymbol{x}_2 - \boldsymbol{U}_m t, 0)$, where $\boldsymbol{U}_m = (\boldsymbol{U}(\boldsymbol{x}_1) + \boldsymbol{U}(\boldsymbol{x}_2))/2$. The more direct use of Taylor's hypothesis, i.e. interpreting the time series as $\tilde{\boldsymbol{u}}(\boldsymbol{x}_1 - \boldsymbol{U}(\boldsymbol{x}_1)t, 0)$ and $\tilde{\boldsymbol{u}}(\boldsymbol{x}_2 - \boldsymbol{U}(\boldsymbol{x}_2)t, 0)$, would obviously be wrong and it would violate the assumption of homogeneity.

2.4. *The isotropic tensor with the von Kármán spectrum*

The symmetry group of isotropic turbulence is simply all rotations and reflections in $\mathbf{R}^3$. As argued in § 2.2 the spectral tensor may be assumed to be real and symmetric because point reflection with respect to the origin, $-\boldsymbol{I}$, is an element in the symmetry group. In the theory of isotropic turbulence the mean field is assumed to be constant, i.e. no shear. Furthermore, if the flow is assumed to be incompressible the spectral tensor can be written as

$$\Phi_{ij}(\boldsymbol{k}) = \frac{E(k)}{4\pi k^4} \left(\delta_{ij} k^2 - k_i k_j\right). \tag{2.16}$$

where $E(k)\mathrm{d}k$ is half the variance of the wind velocity fluctuations whose magnitude of the wave vector is in the range $(k, k + \mathrm{d}k)$, as can be seen by integrating $\Phi_{ii}(\boldsymbol{k})$ over a spherical shell with constant k.

Von Kármán (1948) has suggested the following form of the energy spectrum:

$$E(k) = \alpha \varepsilon^{\frac{2}{3}} L^{\frac{5}{3}} \frac{(Lk)^4}{(1 + (Lk)^2)^{\frac{17}{6}}}, \tag{2.17}$$

where ε is the rate of viscous dissipation of specific turbulent kinetic energy and L is a lengthscale. The empirical value of α is approximately 1.7. Using (2.7) to derive the one-point spectra, we get

$$F_1(k_1) = \frac{9}{55}\alpha\varepsilon^{\frac{2}{3}}\frac{1}{\left(L^{-2}+k_1^2\right)^{\frac{5}{6}}} \tag{2.18}$$

and for the v- and w-spectra:

$$F_i(k_1) = \frac{3}{110}\alpha\varepsilon^{\frac{2}{3}}\frac{3L^{-2}+8k_1^2}{\left(L^{-2}+k_1^2\right)^{\frac{11}{6}}} \quad \text{for } i = 2,3. \tag{2.19}$$

All the one-point cross-spectra are zero.

The lengthscale, L, in the one-point spectra can be calculated from $F_i(0)$. In the atmosphere, however, the spectra at the very lowest wavenumbers vary considerably owing to non-stationarity and large-scale phenomena, which are not of interest here. A better way of characterizing L is by the maximum of $k_1F_i(k_1)$. Denoting the wavenumber at maximum of $k_1F_i(k_1)$ by $1/L_{max,i}$ we get

$$L_{max,1} = \left(\frac{2}{3}\right)^{\frac{1}{2}} L \approx 0.816L \tag{2.20}$$

and

$$L_{max,i} = \frac{2}{(6+3\sqrt{5})^{\frac{1}{2}}}L \approx 0.561L \qquad \text{for } i = 2,3, \tag{2.21}$$

so the maximum of $k_1F_i(k_1)$ occurs when k_1 is slightly larger than $1/L$.

The variances can easily be calculated from either (2.17), (2.18) or (2.19) using (2.10):

$$\sigma_{\text{iso}}^2 = \sigma_{11}^2 = \sigma_{22}^2 = \sigma_{33}^2 = \frac{9}{55}\frac{\pi^{\frac{1}{2}}\Gamma\left(\frac{1}{3}\right)}{\Gamma\left(\frac{5}{6}\right)}\alpha\varepsilon^{\frac{2}{3}}L^{\frac{2}{3}} \approx 0.688\alpha\varepsilon^{\frac{2}{3}}L^{\frac{2}{3}}. \tag{2.22}$$

All the co-variances are of course zero.

The advantage of the isotropic turbulence model is that it describes the spectra and cross-spectra well for high frequencies or small distances compared to the lengthscale of the turbulence. Furthermore, the cross-spectra can be calculated analytically in terms of Bessel functions for the von Kármán energy spectrum, (2.17), or even more simply for the $-\frac{5}{3}$ power law spectrum (Harris 1970; Kristensen & Jensen 1979).

The property of isotropic turbulence that the variances σ_u^2, σ_v^2 and σ_w^2 must all be equal is not supported by data. In fact $\sigma_w^2/\sigma_u^2 \approx 0.25$ and $\sigma_v^2/\sigma_u^2 \approx 0.5$–$0.7$ depending on the averaging time (usually $\approx$ 10 minutes for meteorological measurements). Isotropy also implies that χ_{13} must be zero which is certainly not the case at the lower frequencies (see the dot-dashed line in figure 7).

3. The velocity tensor for shear flow

In this section we sketch the development of two models of the spectral velocity tensor for neutral atmospheric surface-layer turbulence (see Figure 2). We have argued that by neglecting the rotation of the Earth and the effect of gravity and by assuming a linear mean velocity shear, the statistics of the flow has only the four elements of (2.14) as a symmetry group. Our plan is to use RDT to estimate the effect of shear on the turbulence. RDT gives an equation for the evolution or the

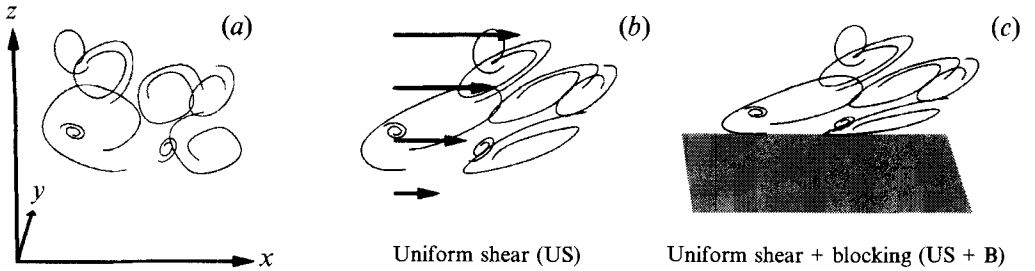

FIGURE 2. Sketch of the investigated models. (*a*) Both models are based on isotropic turbulence with the von Kármán energy spectrum (§ 2.4). (*b*) The effect of shear is modelled by rapid distortion theory in § 3.2. (*c*): In addition blocking by the surface is modelled by 'inhomogeneous rapid distortion theory' (Lee & Hunt 1989, see § 3.3).

'stretching' of the spectral tensor. If the initial conditions can be represented by the isotropic von Kármán tensor, (2.16), with the energy spectrum (2.17), then the tensor $\Phi_{ij}(\boldsymbol{k}, t)$ will become more and more 'anisotropic' with time.

The linearization implied by RDT is unrealistic, however; at some point (in time) the stretched eddies will break up. We shall use this picture to make $\Phi_{ij}(\boldsymbol{k}, t)$ stationary, i.e. not dependent on time. We postulate that eddies of linear dimension $\approx |\boldsymbol{k}|^{-1}$ (or more precisely the Fourier modes) are stretched by the shear over a time which is proportional to their lifetime. The lifetime τ is

$$\tau(k) \propto \varepsilon^{-\frac{1}{3}} k^{-\frac{2}{3}}, \tag{3.1}$$

pertaining, at least in the inertial subrange, to eddies with wave vector magnitude $k = |\boldsymbol{k}|$ (Landau & Lifshitz 1987, § 33).

The basic postulate of this paper is that the *stationary* spectral tensor

$$\Phi_{ij}(\boldsymbol{k}) \equiv \Phi_{ij}(\boldsymbol{k}, \tau(k)) \tag{3.2}$$

describes the surface-layer turbulence well. The combination of RDT and scale-dependent eddy lifetimes has previously been used by Derbyshire & Hunt (1993).

Maxey (1982) has described a similar model with the exception that the lifetime τ was assumed to be constant for all wavevectors. ($\tau \mathrm{d}U/\mathrm{d}z$ is called 'the equilibrium value of the effective distortion strain' by Maxey 1982.) Maxey's model gives a reasonable, but not perfect, description of the ratios among σ_u^2, σ_v^2, σ_w^2 and $\langle uw \rangle$ for turbulent shear flows. There are two grave drawbacks when the model of Maxey (1982) is used to calculate spectra:

(i) The uw-cross-spectrum in the inertial subrange decays as $k_1^{-\frac{5}{3}}$ whereas Wyngaard & Coté (1972) observe and give scaling arguments for $k_1^{-\frac{7}{3}}$.

(ii) For typical values of the effective distortion strain the model predicts $F_u/F_w \approx 7$ in the inertial subrange whereas it should be $F_u/F_w = \frac{3}{4}$ (see figures 7 and 10).

The models presented here do not suffer from these shortcomings.

Several alternative expressions for the eddy lifetime outside the inertial subrange will be discussed in § 3.1. Only an outline of the derivation of the Uniform Shear model (US) will be given in § 3.2 since the basic equations of rapid distortion theory have been given by Townsend (1976). The modification of the model by blocking by the surface (US+B) is given in § 3.3.

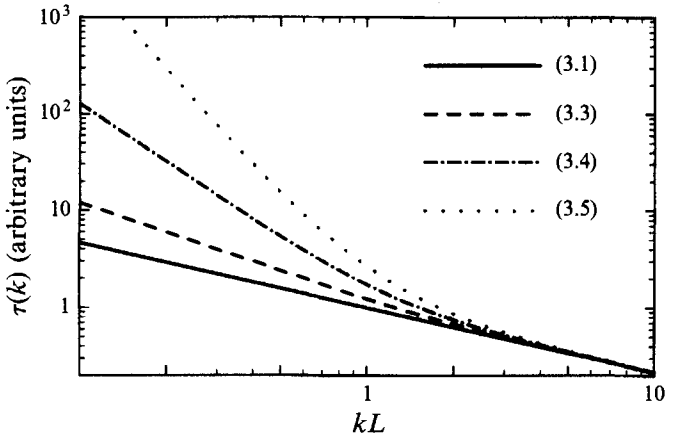

FIGURE 3. Eddy lifetimes as functions of the magnitude of the wave vector. The lifetimes given by (3.3) give the most realistic results.

3.1. *Eddy lifetimes*

At scales larger than the inertial subrange (3.1) is not necessarily valid. We construct an alternative model for the 'eddy lifetime' assuming that the destruction of an eddy with size k^{-1} is mainly due to eddies comparable to or smaller than k^{-1}. The characteristic velocity of these eddies may be expressed as $\approx \left(\int_k^\infty E(p)\mathrm{d}p\right)^{\frac{1}{2}}$, and we simply assume the lifetime to be proportional to the size k^{-1} divided by this velocity:

$$\tau(k) \propto k^{-1}\left(\int_k^\infty E(p)\mathrm{d}p\right)^{-\frac{1}{2}}$$

$$\propto k^{-\frac{2}{3}}\left[{}_2F_1\left(\frac{1}{3},\frac{17}{6};\frac{4}{3};-(kL)^{-2}\right)\right]^{-\frac{1}{2}} \propto \begin{cases} k^{-\frac{2}{3}} & \text{for } k \to \infty \\ k^{-1} & \text{for } k \to 0 \end{cases}, \qquad (3.3)$$

where we have chosen E as the von Kármán energy spectrum (2.17) and where ${}_2F_1$ is the hypergeometric function.

Comte-Bellot & Corrsin (1971, equation 99) give another lifetime model which has the right asymptotic behaviour for $k \to \infty$, the 'coherence-destroying diffusion time' :

$$\tau_D(k) \propto k^{-2}\left[\int_k^\infty p^{-2}E(p)\mathrm{d}p\right]^{-\frac{1}{2}}$$

$$\propto k^{-\frac{2}{3}}\left[{}_2F_1\left(\frac{4}{3},\frac{17}{6};\frac{7}{3};-(kL)^{-2}\right)\right]^{-\frac{1}{2}} \propto \begin{cases} k^{-\frac{2}{3}} & \text{for } k \to \infty \\ k^{-2} & \text{for } k \to 0 \end{cases}, \qquad (3.4)$$

which was constructed as the square of the eddy size divided by a k-dependent 'turbulent viscosity'.

Further, the inverse 'eddy-damping rate'

$$\tau_E(k) \propto \left(k^3E(k)\right)^{-\frac{1}{2}} \propto \begin{cases} k^{-\frac{2}{3}} & \text{for } k \to \infty \\ k^{-\frac{7}{2}} & \text{for } k \to 0 \end{cases} \qquad (3.5)$$

is used by Lesieur (1987) in eddy-damped quasi-normal theories of turbulence as a characteristic nonlinear relaxation time.

All these lifetime models are shown in figure 3 normalized such that they coincide in the inertial subrange. It turns out that σ_u^2 becomes infinite using (3.4) or (3.5), while

(3.1) and (3.3) give reasonable results. It also turns out that the spectra calculated from (3.3) fit the data better than (3.1) for which reason (3.3) is used in the rest of this paper. Some support for (3.3) may be found in Panofsky *et al.* (1982) who measured eddy 'response times' of eddies in the neutral atmospheric surface layer. Also Kristensen & Kirkegaard (1987) were compelled to use (3.3) rather than (3.4) or (3.5) in their theoretical model of the growth of a puff in a turbulent fluid.

It is convenient to write (3.3) as

$$\tau(k) = \Gamma \left(\frac{\mathrm{d}U}{\mathrm{d}z}\right)^{-1} (kL)^{-\frac{2}{3}} \left[{}_2F_1\left(\frac{1}{3}, \frac{17}{6}; \frac{4}{3}; -(kL)^{-2}\right)\right]^{-\frac{1}{2}}, \tag{3.6}$$

where Γ is a parameter to be determined.

3.2. *The uniform shear model*

The flow field is decomposed into a mean and fluctuating part

$$\tilde{\boldsymbol{u}} = \boldsymbol{U} + \boldsymbol{u}, \tag{3.7}$$

where $\boldsymbol{U}$ is given by (2.13). When appropriate we shall use the more general $U_i(\boldsymbol{x}) = x_j \partial U_i/\partial x_j$, where $\partial U_i/\partial x_j$ is a constant tensor, instead of (2.13). The Navier–Stokes equation for an incompressible fluid may be written as

$$\frac{\partial \tilde{u}_i}{\partial t} + \tilde{u}_j \frac{\partial \tilde{u}_i}{\partial x_j} = -\frac{1}{\rho}\frac{\partial p}{\partial x_i} + \nu \frac{\partial^2 \tilde{u}_i}{\partial x_j \partial x_j}, \tag{3.8}$$

assuming the kinematic viscosity ν constant and neglecting gravity and the rotation of the Earth. Upon elimination of the pressure by taking the divergence on both sides of (3.8) and after decomposition in means and fluctuations according to (3.7) we drop the nonlinear and viscous terms and Fourier transform the resulting equation. Defining the 'average total derivative' of the velocity as

$$\frac{\mathrm{D}u_i}{\mathrm{D}t} = \frac{\partial u_i}{\partial t} + U_j \frac{\partial u_i}{\partial x_j} = \frac{\partial u_i}{\partial t} + x_k \frac{\partial U_j}{\partial x_k}\frac{\partial u_i}{\partial x_j}$$

and interpreting the rate of change of wavenumber, $\mathrm{d}k_k/\mathrm{d}t$, by

$$\frac{\mathrm{d}k_k}{\mathrm{d}t} = -k_j \frac{\partial U_j}{\partial x_k} \tag{3.9}$$

the Fourier representation of the average total derivative of the velocity field may be written as

$$\frac{\mathrm{D}u_i(\boldsymbol{x},t)}{\mathrm{D}t} = \int \mathrm{e}^{\mathrm{i}\boldsymbol{k}\cdot\boldsymbol{x}} \left\{\left(\frac{\partial}{\partial t} + \frac{\mathrm{d}k_k}{\mathrm{d}t}\frac{\partial}{\partial k_k}\right)\mathrm{d}Z_i(\boldsymbol{k},t)\right\} = \int \mathrm{e}^{\mathrm{i}\boldsymbol{k}\cdot\boldsymbol{x}} \left\{\frac{\mathrm{D}\mathrm{d}Z_i(\boldsymbol{k},t)}{\mathrm{D}t}\right\}, \tag{3.10}$$

where we have implicitly defined $\mathrm{D}/\mathrm{D}t$ acting on a function of wavenumber and time. Combining this expressions with the linearized and Fourier-transformed version of (3.8) we get

$$\frac{\mathrm{D}\mathrm{d}Z_i(\boldsymbol{k},t)}{\mathrm{D}t} = \frac{\mathrm{d}U}{\mathrm{d}z}\left\{-\delta_{i1} + 2\frac{k_i k_1}{k^2}\right\}\mathrm{d}Z_3(\boldsymbol{k},t), \tag{3.11}$$

which is the basic rapid distortion equation for shear flow. The differential equations (3.9) and (3.11) are easily solved given the initial conditions $\boldsymbol{k}(0) = \boldsymbol{k}_0 = (k_1, k_2, k_{30})$ and $\mathrm{d}\boldsymbol{Z}(\boldsymbol{k}_0, 0)$. Instead of time, t, we shall use the non-dimensional time, β, defined as

$$\beta = \frac{\mathrm{d}U}{\mathrm{d}z}t. \tag{3.12}$$

First (3.9) is solved using the mean flow (2.13) giving

$$\boldsymbol{k}(t) = (k_1, k_2, k_3) \quad \text{where } k_3 = k_{30} - \beta k_1. \tag{3.13}$$

The solution to (3.11) is then

$$\mathrm{d}\boldsymbol{Z}(\boldsymbol{k}, \beta) = \begin{bmatrix} 1 & 0 & \zeta_1 \\ 0 & 1 & \zeta_2 \\ 0 & 0 & k_0^2/k^2 \end{bmatrix} \mathrm{d}\boldsymbol{Z}(\boldsymbol{k}_0, 0), \tag{3.14}$$

where

$$\zeta_1 = \left[C_1 - \frac{k_2}{k_1} C_2\right], \quad \zeta_2 = \left[\frac{k_2}{k_1} C_1 + C_2\right] \tag{3.15}$$

with

$$C_1 = \frac{\beta k_1^2 (k_0^2 - 2k_{30}^2 + \beta k_1 k_{30})}{k^2 (k_1^2 + k_2^2)} \tag{3.16}$$

and

$$C_2 = \frac{k_2 k_0^2}{(k_1^2 + k_2^2)^{\frac{3}{2}}} \arctan\left[\frac{\beta k_1 (k_1^2 + k_2^2)^{\frac{1}{2}}}{k_0^2 - k_{30} k_1 \beta}\right]. \tag{3.17}$$

The equations (3.13) and (3.14) give the temporal evolution of individual Fourier modes.

Given the initial second-order statistics $\Phi_{ij}(\boldsymbol{k}_0, 0) = \Phi_{ij}^{iso}(\boldsymbol{k}_0)$ as the isotropic von Kármán tensor, (2.16), with energy spectrum, (2.17), we then have an explicit expression for $\Phi_{ij}(\boldsymbol{k}, t)$ (using (2.5)).

To make a stationary model we use (3.6) and (3.2) discussed in the beginning of this section, i.e. we substitute t with τ given by (3.6). For the 33-component we get

$$\Phi_{33}(\boldsymbol{k}) = \Phi_{33}^{iso}(\boldsymbol{k}_0) \frac{k_0^4}{k^4} = \frac{E(k_0)}{4\pi k^4} (k_1^2 + k_2^2), \tag{3.18}$$

where Φ_{33}^{iso} refers to the isotropic von Kármán tensor and E to the energy spectrum (2.17). The other components become

$$\Phi_{11}(\boldsymbol{k}) = \frac{E(k_0)}{4\pi k_0^4} \left(k_0^2 - k_1^2 - 2k_1 k_{30} \zeta_1 + (k_1^2 + k_2^2) \zeta_1^2\right), \tag{3.19}$$

$$\Phi_{22}(\boldsymbol{k}) = \frac{E(k_0)}{4\pi k_0^4} \left(k_0^2 - k_2^2 - 2k_2 k_{30} \zeta_2 + (k_1^2 + k_2^2) \zeta_2^2\right), \tag{3.20}$$

$$\Phi_{12}(\boldsymbol{k}) = \frac{E(k_0)}{4\pi k_0^4} \left(-k_1 k_2 - k_1 k_{30} \zeta_2 - k_2 k_{30} \zeta_1 + (k_1^2 + k_2^2) \zeta_1 \zeta_2\right), \tag{3.21}$$

$$\Phi_{13}(\boldsymbol{k}) = \frac{E(k_0)}{4\pi k_0^2 k^2} \left(-k_1 k_{30} + (k_1^2 + k_2^2) \zeta_1\right), \tag{3.22}$$

and

$$\Phi_{23}(\boldsymbol{k}) = \frac{E(k_0)}{4\pi k_0^2 k^2} \left(-k_2 k_{30} + (k_1^2 + k_2^2) \zeta_2\right). \tag{3.23}$$

The equations (3.18) to (3.23) with (3.6) constitute the uniform shear model (US).

These equations have two differences from the expressions of Townsend (1976) for plane shearing of homogeneous turbulence. The first is the elimination of time by (3.6) and the second and related difference is that we do not use the turbulent viscosity of Townsend, which would make the decay time for all eddies equal, independent

of their sizes. (There are, however, also two typographical errors in (3.12.4) of Townsend (1976): in the innermost brackets in the the expression for Φ_{11}, k_{20} should be changed into k_{30}; the expression for Φ_{13} should be divided by k_0^2.)

3.3. *The effect of blocking by the surface*

The US model presented in §3.2 has the symmetry group (2.14). This implies for example that the one-point cross-spectrum of longitudinal and vertical fluctuation $\chi_{uw}(k_1)$ is real and that $\chi_{vw}(k_1, \Delta y, \Delta z = 0)$ is purely imaginary, i.e. $\phi_{vw}(k_1, \Delta y, \Delta z = 0) = \pm 90°$. As seen from figure 10(*b*) $\mathrm{Im}(\chi_{uw}(k_1))$ is in fact negative, and $\phi_{vw}(k_1, \Delta y, \Delta z = 0)$ is systematically different from $\pm 90°$ for low wavenumbers (see figure 9*b*). This means that the deviation from the reflection symmetry in the y-axis has measurable consequences. In this section we shall modify the US model by incorporating the effect of blocking by the surface which will break this reflection symmetry. The physical assumptions in this section are crude, especially for the atmospheric flows under consideration, but are made to illuminate effect of blocking in a tractable way.

We follow the ideas of Lee & Hunt (1989): they analyse by RDT how homogeneous turbulence in a uniform shear is distorted when a rigid surface at $z = 0$ is suddenly introduced at time $\beta = 0$. As in the US model we ignore viscosity so the only effect of the surface is to block vertical velocity fluctuation. The blocked velocity field $\boldsymbol{u}^B(\boldsymbol{x}, \beta)$ is written as $\boldsymbol{u}^B = \boldsymbol{u} + \boldsymbol{u}^S$, where $\boldsymbol{u}(\boldsymbol{x}, \beta)$ is the homogeneous velocity field from the US model and $\boldsymbol{u}^S$ obeys $w^S(x, y, 0, \beta) = -w(x, y, 0, \beta)$, such that $w^B = 0$ on the surface, and $\boldsymbol{u}^S \to 0$ for $z \to \infty$.

We no longer have homogeneity in the vertical direction and it is appropriate to use Fourier transforms in the two horizontal directions. The two-dimensional Fourier transform of the homogeneous velocity field $u_i(\boldsymbol{x})$ from the US model thus becomes

$$\mathrm{d}\mathscr{Z}_i(k_1, k_2, z, \beta) = \int_{k_3} \mathrm{d}Z_i \mathrm{e}^{\mathrm{i}k_3 z}, \tag{3.24}$$

where $\int_{k_3}$ denotes integration over all the k_3 and $\mathrm{d}Z_i$ is given by (3.14).

Hunt (1973) and Hunt & Graham (1978) show that $\boldsymbol{u}^S$ is irrotational at the initial instant ($\beta = 0$) and has the form

$$\mathrm{d}\mathscr{Z}_3^S(k_1, k_2, z, 0) = -\mathrm{e}^{-z\kappa} \int_{k_3} \mathrm{d}Z_3(\boldsymbol{k}, 0) \tag{3.25}$$

and

$$\mathrm{d}\mathscr{Z}_i^S(k_1, k_2, z, 0) = \mathrm{i}k_i \frac{\mathrm{e}^{-z\kappa}}{\kappa} \int_{k_3} \mathrm{d}Z_3(\boldsymbol{k}, 0) \quad \text{for } i = 1, 2, \tag{3.26}$$

where $\kappa = (k_1^2 + k_2^2)^{\frac{1}{2}}$. From the momentum equation Gartshore *et al.* (1983) derive

$$\mathrm{D}/\mathrm{D}\beta \nabla^2 w^S = 0$$

for a linear shear which implies

$$\mathrm{d}\mathscr{Z}_3^S(k_1, k_2, z, \beta) = -\mathrm{e}^{-z\kappa} \int_{k_3} \mathrm{d}Z_3(\boldsymbol{k}, \beta) = -\mathrm{e}^{-z\kappa} \mathrm{d}\mathscr{Z}_3(k_1, k_2, 0, \beta) \tag{3.27}$$

(see also Durbin 1978).

The other two components of the velocity field may be found from the first two

components of the curl of the linearized momentum equations

$$\frac{\mathrm{D}}{\mathrm{D}\beta}\left(\frac{\partial w^S}{\partial y}-\frac{\partial v^S}{\partial z}\right)=\frac{\partial v^S}{\partial x} \quad \text{and} \quad \frac{\mathrm{D}}{\mathrm{D}\beta}\left(\frac{\partial u^S}{\partial z}-\frac{\partial w^S}{\partial x}\right)=\frac{\partial v^S}{\partial y} \tag{3.28}$$

as it has been done by Lee & Hunt (1989). The results are

$$\mathrm{d}\mathscr{Z}_i^S(k_1,k_2,z,\beta)=\mathrm{i}\frac{k_i}{\kappa}\mathrm{e}^{-z\kappa}\int_{k_3}(1+P_i(z))\,\mathrm{d}Z_3(\boldsymbol{k},\beta), \tag{3.29}$$

where

$$P_1(z)=\frac{k^2k_2^2}{2\kappa^2k_1^2}Q(z) \quad \text{and} \quad P_2(z)=-\frac{k^2}{2\kappa^2}Q(z). \tag{3.30}$$

The function Q is given by

$$\begin{aligned}Q(z)=\mathrm{e}^{\mathrm{i}k_3z}\ \Big\{&\mathrm{e}^{\kappa z}\left[E_1(\kappa z+\mathrm{i}k_{30}z)-E_1(\kappa z+\mathrm{i}k_3z)\right]\\&-\mathrm{e}^{-\kappa z}\left[2\pi\mathrm{i}H(-k_3k_{30})+E_1(-\kappa z+\mathrm{i}k_{30}z)-E_1(-\kappa z+\mathrm{i}k_3z)\right]\Big\},\end{aligned} \tag{3.31}$$

where H is the Heaviside function ($H(x)=1$ for $x>0$ and 0 for $x<0$) and E_1 is the exponential integral function.

Using (3.24), (3.27) and (3.29) and eliminating the time dependence by (3.2) the spectral tensor for the blocked flow now becomes a function of the two horizontal wave vectors and two heights above the surface:

$$\Phi_{ij}^B(k_1,k_2,z_1,z_2)\equiv\frac{\left\langle\left(\mathrm{d}\mathscr{Z}_i(k_1,k_2,z_1)+\mathrm{d}\mathscr{Z}_i^S(k_1,k_2,z_1)\right)^*\left(\mathrm{d}\mathscr{Z}_j(k_1,k_2,z_2)+\mathrm{d}\mathscr{Z}_j^S(k_1,k_2,z_2)\right)\right\rangle}{\mathrm{d}k_1\mathrm{d}k_2} \tag{3.32}$$

from which all spectra and cross-spectra can be derived. As an example the 11-component becomes

$$\begin{aligned}\Phi_{11}^B(k_1,k_2,z_1,z_2)=&\int_{-\infty}^{\infty}\Phi_{11}(\boldsymbol{k})\mathrm{e}^{\mathrm{i}k_3(z_2-z_1)}\\&+\frac{\mathrm{i}k_1}{\kappa}\left\{(1+P_1(z_2))\mathrm{e}^{-\mathrm{i}k_3z_1}\mathrm{e}^{-\kappa z_2}-(1+P_1(z_1))^*\mathrm{e}^{\mathrm{i}k_3z_2}\mathrm{e}^{-\kappa z_1}\right\}\Phi_{13}(\boldsymbol{k})\\&+k_1^2\frac{\mathrm{e}^{-\kappa(z_1+z_2)}}{\kappa^2}(1+P_1(z_1))^*(1+P_1(z_2))\Phi_{33}(\boldsymbol{k})\mathrm{d}k_3.\end{aligned} \tag{3.33}$$

Although being more complicated than the US model, the US+B model does not contain more adjustable parameters since the distance to the surface z is known.

3.4. *Properties of the sheared velocity tensors*

We shall now investigate the basic properties of the sheared velocity tensors, (3.18) to (3.23) and (3.32). The only four (co-)variances which are not zero, i.e. $\sigma_{11}^2=\sigma_u^2$, $\sigma_{22}^2=\sigma_v^2$, $\sigma_{33}^2=\sigma_w^2$ and $\langle uw\rangle$, are calculated numerically by (2.10) and are shown in figure 4(*a*) for the US model as functions of Γ. The model exhibits the ordering $\sigma_u^2>\sigma_v^2>\sigma_w^2$ and a negative co-variance of u and w as observed in neutral flows over homogeneous terrain in the atmosphere. In figure 5(*a*) the (co-)variances from the US+B model (§ 3.3) for $\Gamma=3.5$ are shown. It is seen that σ_w^2 and $\langle uw\rangle$ are attenuated strongly close to the surface. This is not consistent with surface-layer scaling where

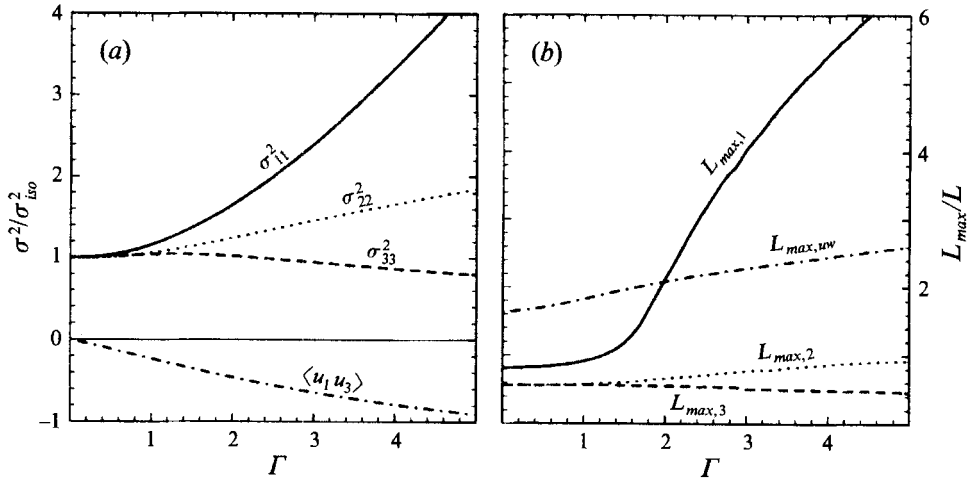

FIGURE 4. Properties of the uniform shear model as functions of the parameter Γ : (*a*) (co-)variances divided by the isotropic variance (2.22); (*b*) lengthscales of (cross-)spectra defined by (3.34) divided by L.

$\langle uw \rangle$ is approximately constant. However, the US+B model may be able to model the surface-layer turbulence within a horizontal slab where $\langle uw \rangle$ is not varying too much.

Another characteristic feature of the one-point (cross-)spectra is the extremum of $k_1 F_i(k_1)$ or $k_1 \mathrm{Re}(\chi_{13}(k_1))$. Assuming isotropy this could be found analytically ((2.20) and (2.21)), but in the sheared case the extremum must be found numerically by integrating (2.7) with $\Delta y = \Delta z = 0$. Defining

$$L_{max,i} \equiv 1/k_{max,i}, \tag{3.34}$$

where $k_{max,i}$ is the solution to

$$\frac{\mathrm{d}}{\mathrm{d}k_1}(k_1 F_i(k_1)) = 0,$$

we get the ordering $L_{max,1} > L_{max,2} > L_{max,3}$ for the US model as seen from figure 4(*b*), which is in at least qualitative agreement with experiments. The lengthscales of the US+B model are strongly attenuated close to the surface as seen from figure 5(*b*).

4. Experimental validation

To test the tensor models described in § 3 our strategy is as follows:

(i) We determine the three parameters L, Γ and $\alpha\varepsilon^{\frac{2}{3}}$ of each of the models from the four non-zero spectra measured in *one* point, namely $F_u(k_1)$, $F_v(k_1)$, $F_w(k_1)$ and $F_{uw}(k_1) = \mathrm{Re}(\chi_{uw}(k_1))$. (In the case of the model in § 3.3 $\mathrm{Im}(\chi_{uw}(k_1))$ is also non-zero.)

(ii) Then we predict all *two-point* cross-spectra or coherences.

(iii) Finally, we compare the predicted and measured two-point cross-spectra.

The easiest way to extract the parameters from the measured spectra would be to estimate the lengthscales, defined as the reciprocal of the wavenumber that extremizes $k_1 F(k_1)$, and then determine Γ and L from figure 4(*b*) in case of the US model. The measured variances could then be used the estimate $\alpha\varepsilon^{\frac{2}{3}}$ from figure 4(*a*) and (2.22), or alternatively the parameter could be determined from $\lim_{k_1 \to \infty} k_1^{\frac{5}{3}} F_1(k_1)$ which for

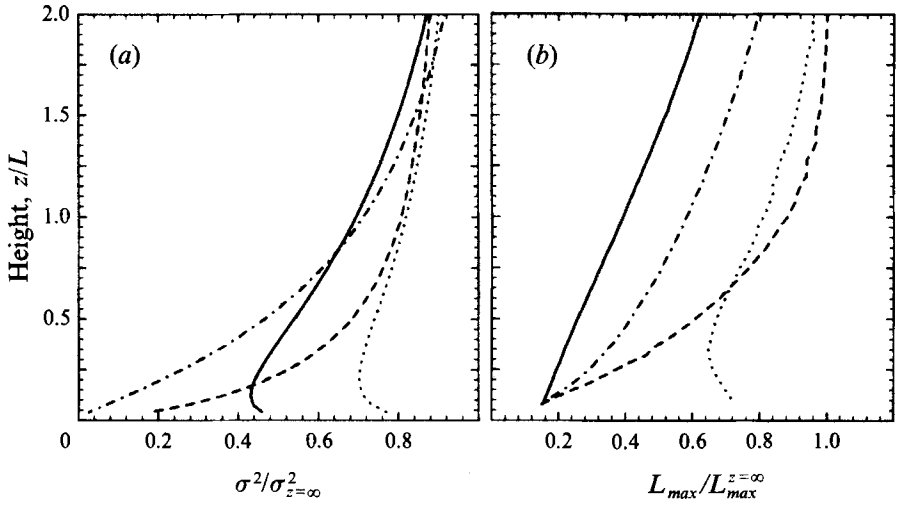

FIGURE 5. The effect of blocking on the (co-)variances (*a*) and lengthscales (*b*) as function of distance to the surface normalized by the unblocked values. The lifetime parameter Γ is 3.5. See figure 4 for labels to the curves.

$i = 1$ is $\frac{9}{55}\alpha\varepsilon^{\frac{2}{3}}$ and for $i = 2, 3$ is $\frac{12}{55}\alpha\varepsilon^{\frac{2}{3}}$, see (2.18) and (2.19), for which the limits still are valid in the sheared case because the distortion tends to zero for large wavenumbers according to (3.1). There are, however, several reasons not to proceed in that way. Firstly, because the time series available are of limited length the estimated spectra appear 'ragged' and the global extrema are greatly influenced by random spikes in the spectra. Secondly, the measured variances depend on the filtering by the instruments in the high-frequency end and on large-scale phenomena in the low-frequency end, which can be caused by small departures from neutral stratification. We do not want to model these very low-frequency phenomena.

Instead we find the parameters by performing a χ^2-fit of the models to the data. In other words we minimize

$$\chi^2(\Gamma, L, \alpha\varepsilon^{\frac{2}{3}}) = \sum_{j=1}^{N} \frac{(F_{uw,t}(k_j) - F_{uw}(k_j))^2}{\sigma_u(k_j)\sigma_w(k_j)} + \sum_{i=1}^{3}\sum_{j=1}^{N} \frac{\left(F_{i,t}(k_j) - F_i(k_j)\right)^2}{\sigma_i^2(k_j)}, \tag{4.1}$$

where N is the number of wavenumbers in the estimated spectra. A subscript t means theoretical model values calculated by (2.7) with $\Delta y = \Delta z = 0$, using the tensor models described in § 3. The σ^2 are the variances of the spectral estimates at the given wavenumber, which will be discussed below.

4.1. *Time series analysis*

The spectra are estimated by dividing the time series into a number, n, of 'ensembles' of equal duration. Each segment is Fourier transformed and the spectrum is the average of the absolute square of the Fourier transform over all the ensembles. Cross-spectra are the ensemble average of Fourier amplitude of the first time series times the complex conjugate of the second. The coherence is estimated as the absolute square of the cross-spectrum divided by the product of the estimated spectra, and the phase is the argument of the complex cross-spectrum, in accordance with (2.8) and (2.9), respectively.

Under the assumption that the time series is long compared to the timescale of the

spectrum L/U, the relative standard deviation of the spectral estimate is

$$\frac{\sigma(F_i)}{\langle F_i \rangle} = \frac{1}{n^{\frac{1}{2}}} \tag{4.2}$$

and for the cross-spectrum

$$\frac{\sigma(\chi_{ij})}{(\langle F_i \rangle \langle F_j \rangle)^{\frac{1}{2}}} = \frac{1}{n^{\frac{1}{2}}} \tag{4.3}$$

(Koopmans 1974). Often the spectra are block averaged over, say, n_b consecutive frequencies or wavenumbers in which case the relative standard deviation becomes $(n_b n)^{-\frac{1}{2}}$.

As an example the spectra in figure 7 are made on basis of time series of length 6 h = 21600 s, which are divided into 27 pieces of 800 s. The relative standard deviation is thus $27^{-\frac{1}{2}} \approx 19\%$ at the lower wavenumbers and smaller at higher wavenumbers, where block averaging is applied.

If we use (4.2) and (4.3) in the χ^2-fit, (4.1), the data will be closely fitted at the high wavenumbers but may be fitted poorly at the lower wavenumbers. In practice we have found that constant relative standard deviations give more satisfactory fits.

The statistics of the estimated coherences are more complicated. Kristensen & Kirkegaard (1986) have analysed the problem in depth. We shall use their results derived under the assumption that the segments of the time series are independent of each other. Let coh_n denoted the coherence estimated as described above from n segments of two time series having the true coherence, coh. The (ensemble) average of this stochastic variable is unfortunately not the true coherence, coh, but

$$\langle \mathrm{coh}_n \rangle = \alpha_1 \tag{4.4}$$

with α_1 given by

$$\alpha_1 = 1 - \frac{n-1}{n}(1-\mathrm{coh})^n \, {}_2F_1(n, n; n+1; \mathrm{coh}). \tag{4.5}$$

It can shown that $\langle \mathrm{coh}_n \rangle > \mathrm{coh}$, i.e. the coherence is on average or systematically overestimated, and that $\lim_{n\to\infty} \langle \mathrm{coh}_n \rangle = \mathrm{coh}$. For the number of segments we have used for the estimation of the coherence ($\geqslant 144$) the overestimation is almost insignificant. For example $\langle \mathrm{coh}_{144} \rangle = 0.5017$ for $\mathrm{coh} = 0.5$ and $\langle \mathrm{coh}_{144} \rangle = 0.0168$ for $\mathrm{coh} = 0.01$.

Kristensen & Kirkegaard (1986) found the ensemble variance of the coherence estimate to be

$$\mathrm{Var}(\mathrm{coh}_n) = \alpha_2 - \alpha_1^2, \tag{4.6}$$

where

$$\alpha_2 = 1 - (1-\mathrm{coh})^n(n-1) \times \left\{ \frac{n}{n+1} \, {}_2F_1(n+1, n; n+2; \mathrm{coh}) - \frac{n-2}{n} \, {}_2F_1(n, n; n+1; \mathrm{coh}) \right\} \tag{4.7}$$

which has the property that $\lim_{n\to\infty} \mathrm{Var}(\mathrm{coh}_n) = 0$.

In order to assess the success of the prediction of the coherence we define a 'goodness' parameter

$$G = \frac{\sigma_{\mathrm{coh}}}{\sigma_{\mathrm{coh},t}}, \tag{4.8}$$

which is the ratio of the actual integrated scatter of the data around the predicted

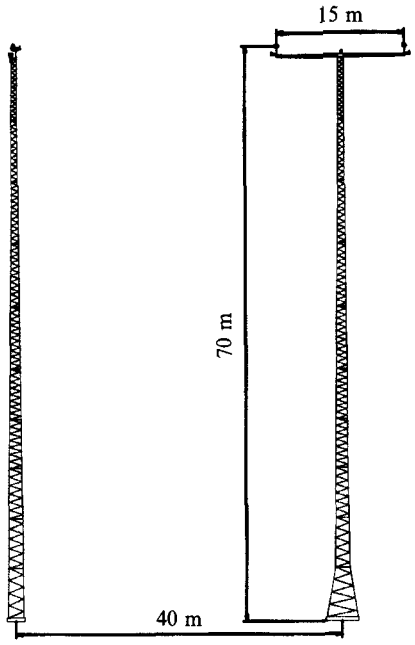

FIGURE 6. The mast array on Sprogø viewed from SSE. The tiny dots at the top of the masts are the omni-directional sonic anemometers.

coherence, σ_{coh}, to the theoretically expected scatter, $\sigma_{\mathrm{coh},t}$. The integrated scatter is

$$\sigma^2_{\mathrm{coh}} = \frac{1}{N}\sum_{i}^{N}(\langle \mathrm{coh}_{n,t}(k_i)\rangle - \mathrm{coh}_n(k_i))^2, \tag{4.9}$$

where $\mathrm{coh}_n(k_i)$ is the coherence estimated from n segments of the time series at the wavenumber k_i, and $\langle \mathrm{coh}_{n,t}(k_i)\rangle$ is the theoretically predicted coherence with the small overestimation added caused by the finite number of degrees of freedom according to (4.4). N is the number of wavenumbers taken into the comparison with data. The expected scatter for a perfect theory is

$$\sigma^2_{\mathrm{coh},t} = \frac{1}{N}\sum_{i}^{N}\mathrm{Var}\left(\mathrm{coh}_{n,t}(k_i)\right), \tag{4.10}$$

where the variance of the predicted coherence is given by (4.6). For a perfect theory the value of G should be close to one.

Finally, we shall also use an approximate expression for the variance of the phase estimate from Kristensen & Kirkegaard (1986):

$$\mathrm{Var}(\varphi) \approx \frac{1-\mathrm{coh}}{2(n-1)\,\mathrm{coh}}\left[1-(1-\mathrm{coh})^{n-1}\right]. \tag{4.11}$$

4.2. *The Great Belt Coherence Experiment*

The construction of the world's largest suspension bridge connecting two islands of Denmark, Funen and Zealand, is about to begin. The suspension bridge will have a main span of 1624 m and the 27 m wide girder deck will rise almost 70 m over the waters of the Great Belt. The girder will be aerodynamically shaped and a large part of the dynamic force on it arises from the turbulence of the wind. The cross-spectrum

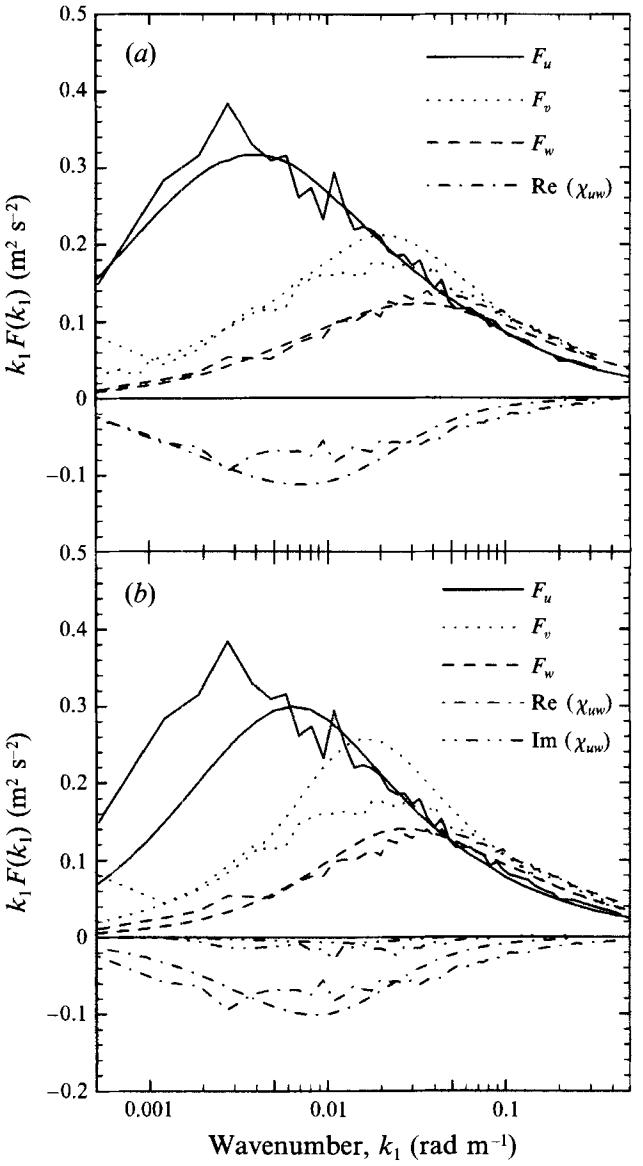

FIGURE 7. Fit of the model spectra (smooth lines) to the data (ragged lines) from the Great Belt Coherence Experiment. The US model is shown in (*a*), US+B in (*b*). Since $\mathrm{Im}(\chi_{uw}) = 0$ for the US model it is only shown in (*b*). The values of the model parameters are given in table 1.

of vertical velocity fluctuations $\chi_{ww}(k_1, \Delta y, 0)$ which give rise to lift forces on the girder, and also χ_{uu}, are of importance for the estimation of dynamic loads on the bridge. Risø National Laboratory was therefore asked to perform an experiment to measure and model the relevant cross-spectra or coherences for the design basis of the Great Belt Bridge.

4.2.1. *Description of the experiment*

In order to conduct the coherence measurements a 70 m high mast was erected 40 m from an existing mast on the easterly spit of Sprogø, an island in the midst

	Great Belt		LAMEX	
	US	US+B	US	US+B
L (m)	61	100	42	67
Γ	3.2	3.8	2.6	3.4
$\alpha\varepsilon^{\frac{2}{3}}$ ($m^{\frac{4}{3}}s^{-2}$)	0.11	0.105	0.095	0.092

TABLE 1. Parameters obtained by fitting models to the data. US: Uniform shear model (§ 3.2), US+B: Uniform shear + blocking effects (§ 3.3). Compare with figures 7 and 10.

	$\Delta y = 15$ m		$\Delta y = 32.5$ m		$\Delta y = 47.5$ m	
Components	US	US+B	US	US+B	US	US+B
uu	1.5	2.1	2.3	1.8	3.7	2.8
vv	2.0	2.7	1.7	3.0	2.0	3.3
ww	3.0	3.7	3.8	3.4	4.4	2.9
uv	1.1	1.1	1.5	1.2	1.8	1.5
uw	4.7	3.3	3.9	2.4	3.7	2.2
vw	1.2	1.0	1.4	1.2	1.7	1.4

TABLE 2. The 'goodness', G, of the coherence prediction given by (4.8). Compare with figures 8 and 9. A perfect prediction has $G = 1$.

of the Great Belt. A 15 m long horizontal boom was mounted symmetrically at the top of the new mast so that the whole construction has the form of a letter 'T'. A Kaijo-Denki DAT-300 omni-directional sonic anemometer was installed at each end of the boom and at the top of the old mast, providing 15.0, 32.5 and 47.5 m horizontal separations between the three co-linear instruments. The mast array is shown in figure 6.

The masts had other instruments to measure velocity and temperature profiles in order to determine the stability and to cross-check the sonic anemometers.

We obtained one year of excellent data from which we can calculate lateral coherences with unsurpassed precision. More details about the experiment including correction for flow distortion by the sonic anemometers may be found in Mann *et al.* (1991).

4.2.2. *Comparison with data*

To test the models we have selected a six hour time series. This series is chosen because the wind direction is virtually perpendicular to the instrument line and the wind speed, which is fluctuating around 22.3 $m\,s^{-1}$ at 70 m above the sea, was the largest for that wind direction during the experiment. The few other runs that were perpendicular to the instrument line and had high wind speeds are analysed in Mann *et al.* (1991). The upstream over-water fetch is uninterrupted for more than 20 km. One-point spectra are calculated as described in § 4.1 and are shown twice in figure 7.

The parameters of the models are found by minimizing (4.1). Keeping in mind that all four non-zero one-points spectra are fitted simultaneously with only *three* parameters the fits for both models are very satisfactory.

The coherences are now predicted by performing the integral (2.7) numerically and using the definition of coherence, (2.8). The numerics of a fast evaluation of (2.7) are described in Mann *et al.* (1991). In table 2 the goodness, G, of the predictions of all possible combinations of velocity components at the three different horizontal

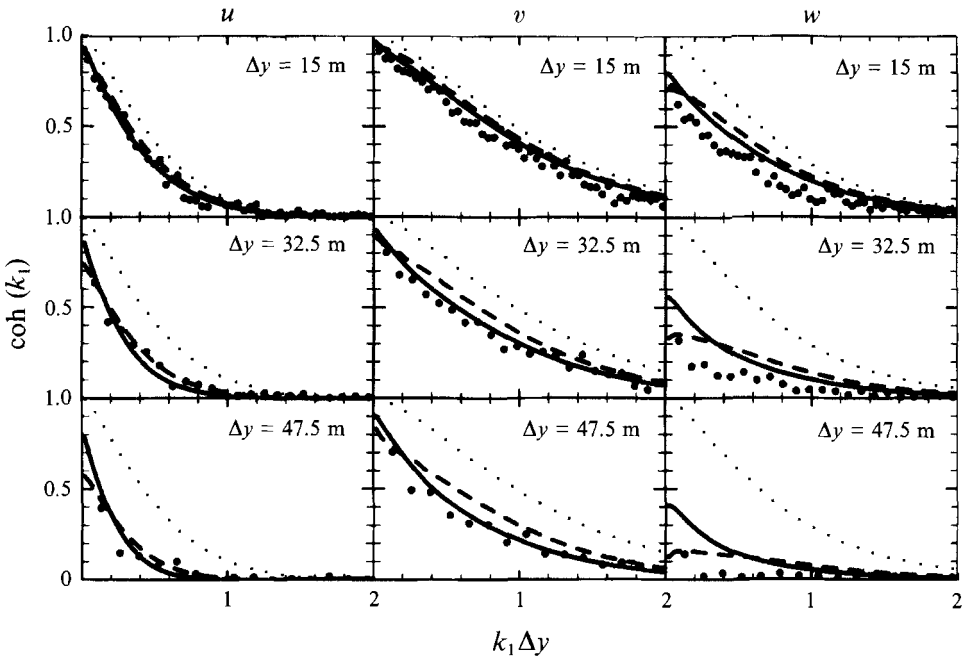

FIGURE 8. Measured (dots) and predicted coherences (solid lines, US; dashed lines, US+B) at all horizontal separations from the Great Belt. The rightmost plot at the top is $\mathrm{coh}_{11}(k_1, 15\ \mathrm{m}, 0)$. The dotted lines are the isotropic inertial-range coherences, i.e. coherences valid for very small Δy (Harris 1970; Kristensen & Jensen 1979). Compare with table 2.

distances for both models are shown. To get an idea of the meaning of G table 2 should be compared to figure 8, where the measured and predicted coherences for some component combinations are plotted.

There is generally a good agreement between measurements and predictions. One of the poorer predictions in figure 8 is by the US model of $\mathrm{coh}_{33}(k_1, 47.5\ \mathrm{m}, 0)$. In this case $G = 4.4$ as seen from table 2 and the US+B model obviously gives a better prediction with $G = 2.9$. Generally, there are otherwise not very large differences between the model predictions. Large departures from the isotropic inertial-subrange coherences are seen at separations as small as $\Delta y = 15$ m.

As an example of coherence between different components of the wind field we have shown coh_{vw} in figure 9(*a*) which is small but significantly larger than zero. The corresponding phase is shown in figure 9(*b*). In the discussion about symmetries in § 2.2 we found that if the turbulent field has the symmetry group (2.14) as the US model, then χ_{vw} is purely imaginary. If this is the case, the phase should be close to $\pm 90°$ which is not found at the lowest wavenumbers in figure 9(*b*). The US+B model gives a slightly better prediction of the phase.

The US tensor model has been tested with other runs from the Great Belt with mean wind speeds in the range 12.5 m s^{-1} to 20 m s^{-1} and with small departures from neutral stability in Mann *et al.* (1991). They used the inertial-subrange lifetime (3.1) instead of (3.6) and got slightly poorer fits to the one-point spectra but the predicted coherences deviated little from the US model with (3.6).

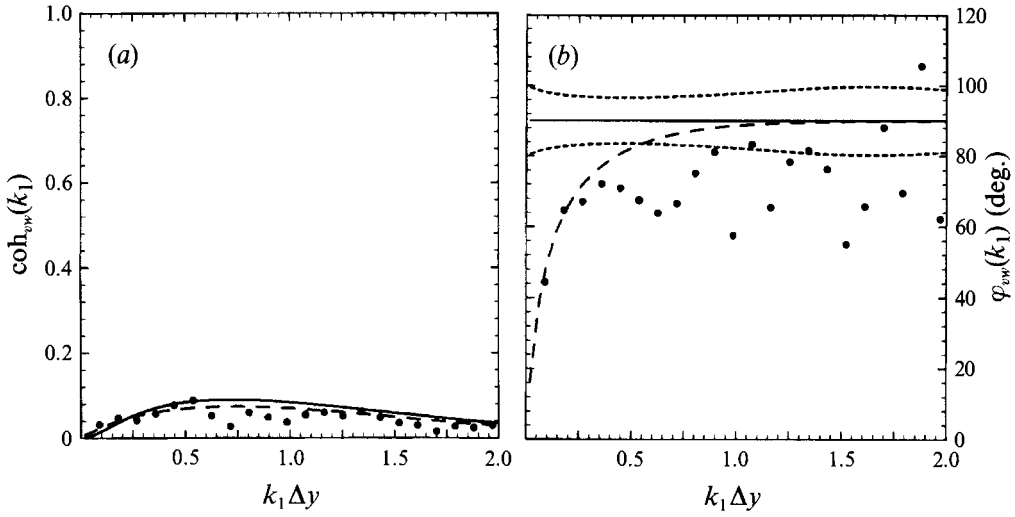

FIGURE 9. Coherence (*a*) and phase (*b*) between the *v*- and the *w*-component for a purely horizontal separation of $\Delta y = 32.5$ m from the Great Belt. The solid curve is the prediction by the US model, the dashed is the US+B model and the dots are experimental values. The short-dashed curves in (*b*) are the theoretical $1 - \sigma$ deviations of the phase from the US model according to (4.11).

46 m	sonic		
30 m	cup	cup	cup
20 m	cup		cup
10 m	cup	cup	cup
Position (y, z)	0 m	20 m	30 m

TABLE 3. Positions of the instruments of the Lammefjord Experiment.

4.3. *The Lammefjord Experiment*

The purpose of the Lammefjord Experiment (LAMEX), which ran from the beginning of June 1987 to the end of June 1988, was to provide wind data suitable both as input for studies of dynamic loads on structures, especially wind turbines, and, as in this study, as a basis for the verification and improvement of atmospheric turbulence models. Courtney (1988) gives a detailed account for the experiment.

4.3.1. *Description of LAMEX*

The experimental site was located at Lammefjord, a reclaimed, flat-bottomed fjord on the Danish island of Zealand. The surrounding land is used for agriculture and lies slightly below sea level. Because of difficulties with drainage, no buildings are found within 2.5 km in the direction of the prevailing southwesterly winds. In this direction the level did not vary more than 1 m. The old sea bed is bounded by a drainage canal beyond which the terrain rises steeply with hills up to approximately 100 m roughly 4 km from the site. The change of roughness 2.5 km upstream of the masts will affect the turbulence measurements above ~ 25 m.

Three masts were erected in a vertical plane perpendicular to the prevailing south-westerly wind direction. Two were 30 m high and the third was 45 m. The positions of the anemometers relative to the base of the 45 m mast are shown in table 3.

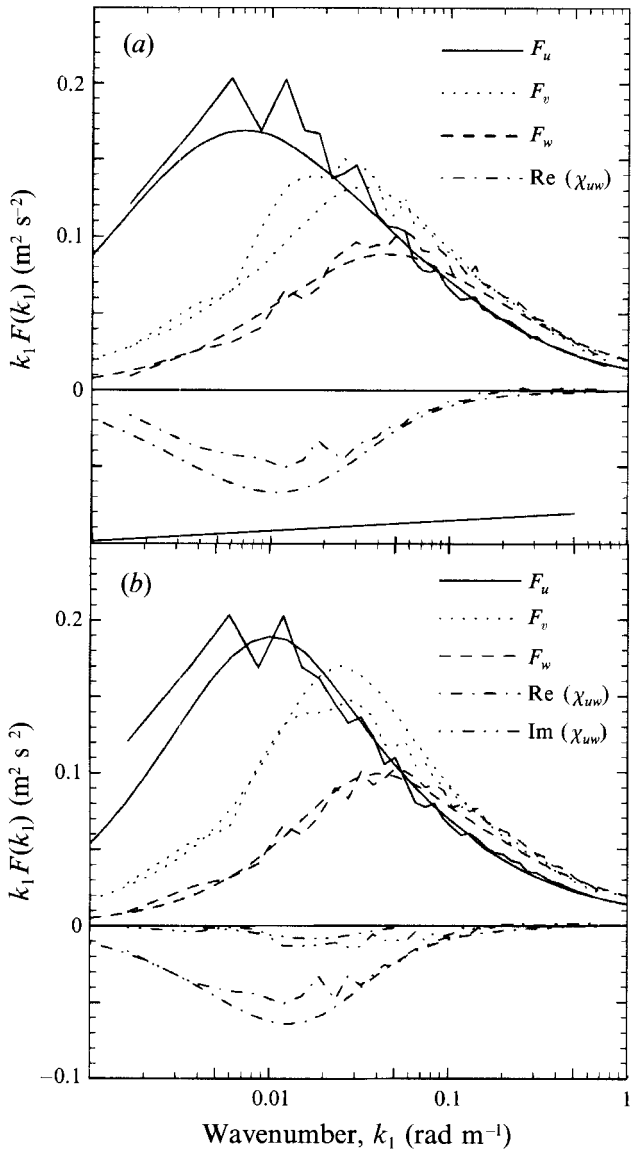

FIGURE 10. Fit of the model spectra (smooth lines) to the data (ragged lines) from the sonic of the Lammefjord Experiment at $z = 46$ m. The US model is shown in (*a*), US+B in (*b*). The values of the model parameters are given in table 1.

The cup anemometers used were the Risø model 70, which has a distance constant of about 1.7 m. At the wavenumbers considered in this study the spectra are unaffected by the low-pass filtering by the cups. The omni-directional sonic anemometer at the top of the highest mast was a Kaijo-Denki model DAT-300. The sonic signal was recorded at 16 Hz and the cups (and some other instruments) were recorded at 8 Hz almost uninterrupted for a year, giving a body of data of approximately 12 Gbytes.

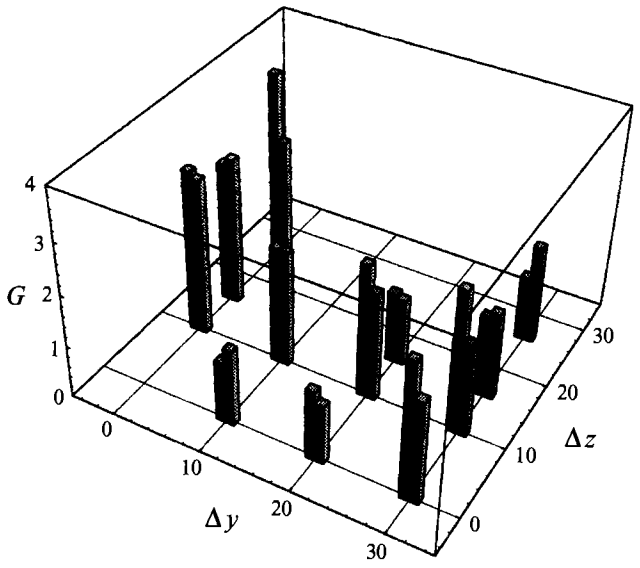

FIGURE 11. 'Goodness' of the predicted *uu*-coherences, G, according to (4.8) as a function of vertical and transversal separation. At each position $(\Delta y, \Delta z)$ the left bar refers to the US model while the right refers to the US+B model. Bars with G close to 1 represent the best predictions.

4.3.2. *Comparison with LAMEX data*

The Lammefjord experiment is not perfectly suited to test our model since the fitting of the one-point component spectra to the model is based on data from the sonic 46 m above the ground while the all the other instruments are at lower heights.

To test our model we have chosen a 10 hour run with mean wind speed around 11 $\mathrm{m\,s^{-1}}$ and direction very close to perpendicular to the mast array. The Richardson number is between 0 and 0.1 at $z = 21$ m, estimated from measured velocity and temperature profiles. Even though the stratification is perhaps slightly stable it is assumed to be sufficiently close to neutral that our model applies. Analysis of more data awaits to clarify the dependence of the spatial structure of turbulence on the stability. The three measured component spectra and the *uw*-cross-spectrum are shown in figure 10 together with the model fit. Again the models account well for the essential features of the spectra. The values of Γ are smaller compared to the Great Belt indicating that the turbulence at the Lammefjord site is more isotropic (see table 1). This may be explained by the limited fetch at the Lammefjord site.

Only instruments from 20 m and above are used to test the model because we consider it too crude to assume a linear wind profile from the sonic at 46 m down to 10 m.

From the parameters obtained from the fits in figure 10 we have predicted all possible coherences between the velocity components of the sonic and the u-components measured by the cups. The 'goodness', G, of the predicted *uu*-coherences is shown in figure 11 as a function of transversal and vertical separation for both the US model and the US+B model. It is seen that the models work well primarily for horizontal separations and that the US+B model generally gives slightly better predictions. The models predict, by a small amount, too large coherences for vertical separations. The consequences for the errors in load calculations on vertical structures depend on the shape of the excited modes. If the typical lengthscale of the mode shape is larger than the 'coherence decay length' the model will predict slightly too high loads.

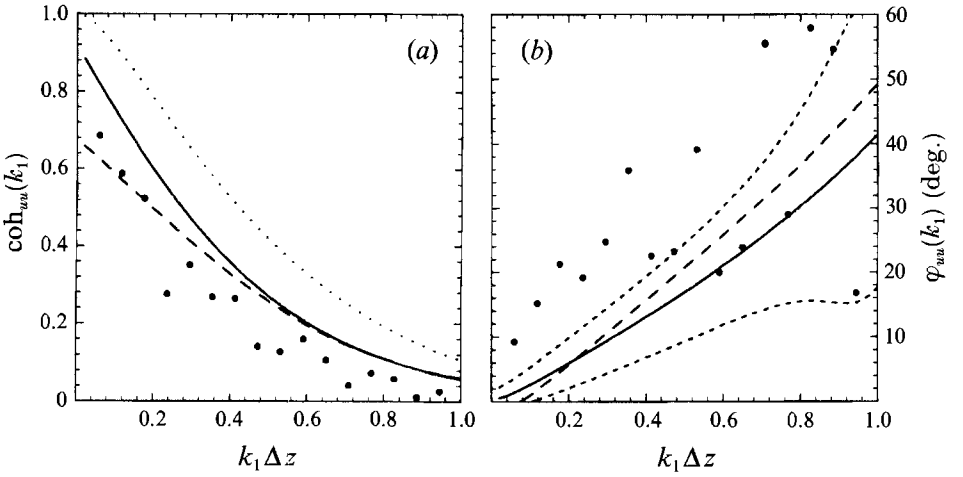

FIGURE 12. *uu*-coherence (*a*) and phase (*b*) for a vertical separation $\Delta z = 26$ m from LAMEX ($z_1 = 20$ m, $z_2 = 46$ m). The dots are measured coherences, the solid curve is the US prediction, the dashed is from the US+B model and the dotted curve is the isotropic inertial-subrange prediction. The short-dashed curves in (*b*) are the theoretical $1 - \sigma$ deviations of the phase from the US model according to (4.11).

	Δy (m)	Δz (m)	G US	G US+B
	20	16	1.9	1.7
uv	30	16	2.3	1.6
	30	26	2.3	1.9
	0	16	3.3	1.0
	0	26	3.3	1.5
uw	20	16	2.2	1.2
	30	16	2.0	2.1
	30	26	2.0	1.4

TABLE 4. 'Goodness' of the predicted *uv*- and *uw*-coherences, G, according to (4.8) for different horizontal and vertical separation, Δy and Δz. Predictions with G closest to one are the best predictions.

The success of the *uv*- and *uw*-coherence predictions is shown in table 4. For the US model the coherences with predominantly horizontal separations again seem to be predicted best, but the US+B model seems to be superior to the US model.

We shall now look at two examples of predicted coherences represented in the bar chart in figure 11 and in table 4. The first is the *uu*-coherence and phase between the sonic at 46 m and a cup directly under the sonic at $z = 20$ m (see table 3) displayed in figure 12. This is a quite poor prediction ($G = 3.6$ for the US model, $G = 2.3$ for US+B); the models, especially the US, are seen to overestimate the coherence systematically.

The phase calculated from the same data is shown in figure 12(*b*), where the scatter is estimated using (4.11). A positive φ here means that the fluctuations at $z = 20$ m come after the fluctuations at $z = 46$ m. The phase and the scatter are well

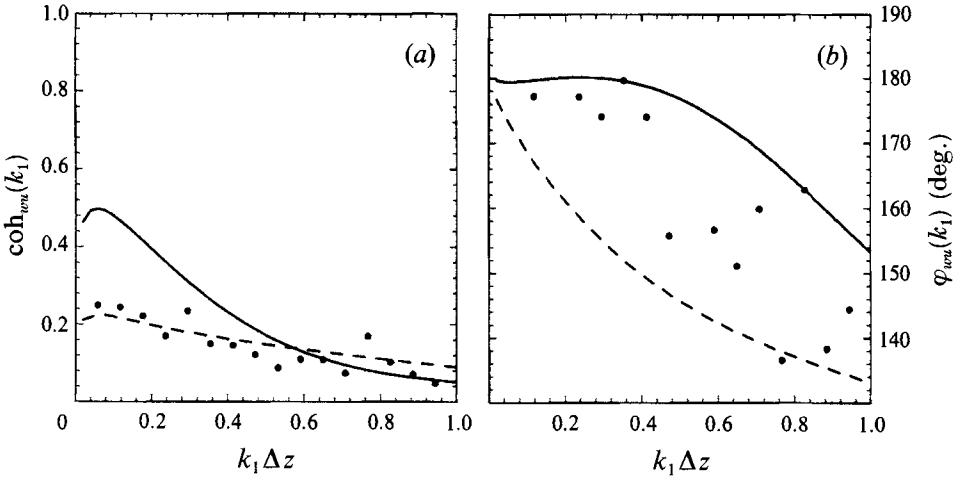

FIGURE 13. *uw*-coherence with w measured at $z = 46$ m and u at 20 m and with zero horizontal separation. See caption to figure 12 for description of symbols.

predicted at the higher wavenumbers while the phase is underestimated at the lowest wavenumbers. The models make quite similar predictions in this case.

The last example (figure 13) shows coherence and phase predicted significantly differently by the two models. The coherence is predicted better by the US+B model which has $G = 1.5$ compared to $G = 3.3$ for the US model. The measured phases are between the two predictions.

5. Conclusion

We have investigated two slightly different models of the spectral tensor of neutral atmospheric surface-layer turbulence which contain only three parameters: a lengthscale L, an eddy lifetime constant Γ and the spectral multiplier in the inertial subrange ($\alpha\varepsilon^{\frac{2}{3}}$). Both models crudely consider the effect of shear on turbulence by using the linearized and inviscid Navier–Stokes equation. The effect of the nonlinear terms is taken into account by including considerations about the lifetime of eddies of different sizes. The simplest model is the uniform shear model (US) (§ 3.2) while the US+B model (§ 3.3) additionally attempts to take into account the effect of blocking by the surface.

We have used two experiments specially designed to measure the spatial structure of turbulence to test the models: the Great Belt Coherence Experiment measuring turbulence over water and the Lammefjord Experiment (LAMEX), which measures turbulence over an almost horizontally homogeneous terrain.

As mentioned in § 2.2, since we have assumed a linear shear, we should only expect the spectral tensors to model eddies with sizes smaller than the scale over which the shear changes appreciably, which in the surface layer is the height above the ground, z. Because of the three adjustable parameters, however, the fit of the model to the *one-point* spectra is good well below $k_1 \approx 2\pi/z$. From these parameters virtually all second-order two point statistics, i.e. coherences, phases etc., are predicted satisfactorily from the models. Both models perform less well for vertical separations (e.g. figure 12) where the departure from a linear profile might be important.

There are only small differences in the predictions made by the US and US+B models, with the notable exception of coherences involving vertical velocity fluctua-

	σ_u^2/q^2	σ_v^2/q^2	σ_w^2/q^2	$-\langle uw\rangle/q^2$
Panofsky & Dutton (1984)	0.53	0.33	0.14	0.09
Other data (Maxey 1982)	0.53	0.28	0.19	0.14
Great Belt	0.54	0.31	0.15	0.11
US model (G.B. parameters)	0.51	0.30	0.19	0.13
US+B model (G.B. parameters)	0.46	0.34	0.20	0.11
Model of Maxey (1982)	0.59	0.34	0.07	0.14
LAMEX†	0.45	0.35	0.20	0.11
US model (LAMEX parameters)	0.47	0.31	0.22	0.13
US+B model (LAMEX parameters)	0.44	0.34	0.22	0.11

† Site is not completely homogeneous.

TABLE 5. Stress ratios from two references, our two experiment and some models. The parameters of the US and US+B models are given in table 1.

tions where the US+B model is superior. For the predicted phases the situation is not that clear (see figures 9*b*, 12*b* and 13*b*). Because the US+B model is more complex than the US model we recommend the latter for engineering purposes, except in cases where the coherence of vertical velocity fluctuations at low frequencies is of particular importance.

The Great Belt Experiment gives a larger value of the lifetime parameter Γ than LAMEX (see table 1). The most plausible cause of the difference is a change of roughness 2.5 km upwind of the LAMEX site as discussed in §§ 4.3.1 and 4.3.2.

This paper differs from previous studies of the application of rapid distortion theory to homogeneous shear flow (Maxey 1982; Townsend 1976; Lee & Hunt 1989) in two respects. Firstly, they do not incorporate 'eddy lifetime' in the spectral tensor models. Maxey's (1982) model assumes that shear acts on all scales with the same strain, in contrast to our model. This has the consequence that the cross-spectrum $F_{uw}(k_1)$ in the inertial subrange is proportional to $k_1^{-\frac{5}{3}}$ while our model predicts $k_1^{-\frac{7}{3}}$ in accordance with Wyngaard & Coté (1972) and that $F_w \ll F_u$ for $k_1 \to \infty$ in contrast to the present models which are isotropic for large k, i.e. $F_w = \frac{4}{3}F_u$ for $k_1 \to \infty$. In relation to this, if the parameters of the model of Maxey (1982) are adjusted to fit the observed shear stress ratio $-\langle uw\rangle/q^2 = 0.14$ (q^2 is $\sigma_u^2 + \sigma_v^2 + \sigma_w^2$) then the derived normalized variances of the three velocity components are not well predicted. In table 5 normalized variances and shear stresses from homogeneous shear flow measurements and models are displayed. It is seen that a closer comparison is found than that by Maxey (1982). The model by Maxey (1982) predicts the ratio σ_v^2/σ_w^2 to be 4.9 while ours gives values in the range 1.4 to 1.7, in better agreement with data. The other difference from the previous studies is that we not only use one-point but also emphasize two-point statistics such as coherences and phases in our experimental validation.

Finally, it should be noted that we have no formal justification to apply rapid distortion theory to stationary and homogeneous flows. The reader may find discussions of this point elsewhere (Townsend 1976; Maxey 1982; Savill 1987; Hunt & Carruthers 1990). The purpose of paper is solely to present the models and make a detailed comparison with data.

The author acknowledges J. C. R. Hunt for suggesting the analysis in § 3.3. I thank Dr Michael S. Courtney and others at the Risø National Laboratory for the excellent experiments, the A/S Storebæltsforbindelsen for financing the Great Belt Coherence Experiment and the Commission of the European Communities Directorate-General for Science, Research and Development for funding the Lammefjord Experiment (LAMEX). The author is grateful to Drs Leif Kristensen and Peter Kirkegaard (both from Risø) for many fruitful discussions and to Professor Steen Krenk of the University of Aalborg for his useful comments to the manuscript. Thanks to suggestions from Drs Jack Herring and Don Lenschow of the National Center for Atmospheric Research in Boulder, Colorado the manuscript has been improved in several ways. The author acknowledges the financial support from The Danish Research Academy during this study.

REFERENCES

BATCHELOR, G. K. 1953 *The Theory of Homogeneous Turbulence.* Cambridge University Press.

CHANDRASEKHAR, S. 1950 The theory of axisymmetric turbulence. *Phil. Trans. R. Soc. Lond.* A **242**, 557–577.

COMTE-BELLOT, G. & CORRSIN, S. 1971 Simple Eulerian time correlation of full- and narrow-band velocity signals in grid-generated, 'isotropic' turbulence. *J. Fluid Mech.* **48**, 273–337.

COURTNEY, M. S. 1988 An atmospheric turbulence data set for wind turbine research. In *Wind Energy Conversion, Proc. 1988 BWEA Wind Energy Conf.* (ed. D. J. Milborrow), pp. 89–94. Mech. Engng Publ.

DAVENPORT, A. G. 1977 The prediction of the response of structures to gusty wind. In *Safety of Structures Under Dynamic Loading* (ed. I. Holland, D. Kavlie, G. Moe & R. Sigbjörnsson), pp. 257–284. Norwegian Institute of Technology, Trondheim.

DERBYSHIRE, S. H. & HUNT, J. C. R. 1993 Structure of turbulence in stably stratified atmospheric boundary layers; comparison of large eddy simulations and theoretical models. In *Waves and Turbulence in Stably Stratified Flows* (ed. S. D. Mobbs & J. C. King), pp. 23–59. Clarendon.

DURBIN, P. A. 1978 Rapid distortion theory of turbulent flows. PhD thesis, University of Cambridge.

GARTSHORE, I. S., DURBIN, P. A. & HUNT, J. C. R. 1983 The production of turbulent stress in a shear flow by irrotational fluctuations. *J. Fluid Mech.* **137**, 307–329.

HARRIS, I. 1970 The nature of the wind. *Proc. Seminar at Inst. Civil Engrs, June 1970.*

HUNT, J. C. R. 1973 A theory of turbulent flow round two-dimensional bluff bodies. *J. Fluid Mech.* **61**, 625–706.

HUNT, J. C. R. & CARRUTHERS, D. J. 1990 Rapid distortion theory and the 'problems' of turbulence. *J. Fluid Mech.* **212**, 497–532.

HUNT, J. C. R. & GRAHAM, J. M. R. 1978 Free-stream turbulence near plane boundaries. *J. Fluid Mech.* **84**, 209–235.

HUNT, J. C. R., MOIN, P., LEE, M., MOSER, R. D., SPALART, P., MANSOUR, N. N., KAIMAL, J. C. & GAYNOR, E. 1989 Cross correlation and length scales in turbulent flows near surfaces. In *Advances in Turbulence*, vol. 2, pp. 128–134, (ed. H.-H. Fernholz & H. E. Fiedler). Springer.

IZUMI, Y. 1971 Kansas 1968 field program data report. *Environmental Research Papers*, No. 379, AFCRL–72–0041, Air Force Cambridge Research Laboratories, Bedford, Massachusetts.

KÁRMÁN, T. VON 1948 Progress in the statistical theory of turbulence. *Proc. Nat. Akad. Sci.* **34**, 530–539.

KOOPMANS, L. H. 1974 *The Spectral Analysis of Time Series.* Academic.

KRISTENSEN, L. & JENSEN, N. O. 1979 Lateral coherence in isotropic turbulence and in the natural wind. *Boundary-Layer Met.* **17**, 353–373.

KRISTENSEN, L. & KIRKEGAARD, P. 1986 Sampling problems with spectral coherence. *Risø Rep.* R–526, 63 pp.

KRISTENSEN, L. & KIRKEGAARD, P. 1987 Puff kinematics. *Risø Rep.* R–548, 88 pp.

KRISTENSEN, L., LENSCHOW, D. H., KIRKEGAARD, P. & COURTNEY, M. S. 1989 The spectral velocity tensor for homogeneous boundary-layer turbulence. *Boundary-Layer Met.* **47**, 149–193.

LANDAU, L. D. & LIFSHITZ, E. M. 1987 *Fluid Mechanics.* Pergamon.

LARSEN, A. (ed.) 1992 *Proc. Intl Symp. on Aerodynamics of Large Bridges*, 305 pp. Balkema.

LEE, M. J. & HUNT, J. C. R. 1989 The structure of sheared turbulence near a plane boundary. *7th Symp. on Turbulent Shear Flows, Stanford.*

LESIEUR, M. 1987 *Turbulence in Fluids.* Martinus Nijhoff.

LUMLEY, J. L. 1970 *Stochastic Tools in Turbulence.* Academic.

MANN, J., KRISTENSEN, L. & COURTNEY, M. S. 1991 The great belt coherence experiment – A study of atmospheric turbulence over water. *Risø Rep.* R–596, 51 pp.

MAXEY, M. R. 1982 Distortion of turbulence in flows with parallel streamlines. *J. Fluid Mech.* **124**, 261–282.

PANOFSKY, H. A. & DUTTON, J. A. 1984 *Atmospheric Turbulence.* John Wiley & Sons.

PANOFSKY, H. A., LARKO, D., LIPSCHUTZ, R., STONE, G., BRADLEY, E. F., BOWEN, A. J. & HØJSTRUP, J. 1982 Spectra of velocity components over complex terrain. *Q. J. R. Met. Soc.* **108**, 215–230.

SAVILL, A. M. 1987 Recent developments in rapid-distortion theory. *Ann. Rev. Fluid Mech.* **19**, 531–575.

SCHMIDT, H. & SCHUMANN, U. 1989 Coherent structure of the convective boundary layer derived from large-eddy simulations. *J. Fluid Mech.* **200**, 511–562.

SREENIVASAN, K. R. & NARASIMHA, R. 1978 Rapid distortion of axisymmetric turbulence. *J. Fluid Mech.* **84**, 497–516.

TENNEKES, H. & LUMLEY, J. L. 1972 *A First Course in Turbulence.* MIT Press.

TOWNSEND, A. A. 1976 *The Structure of Turbulent Shear Flow*, 2nd edn. Cambridge University Press.

WYNGAARD, J. C. & COTÉ, O. R. 1972 Co-spectral similarity in the atmospheric surface layer. *Q. J. R. Met. Soc.* **98**, 590–603.